

# Planar controlled gliding, tumbling and descent

P. Paoletti<sup>1</sup> and L. Mahadevan<sup>1,2,†</sup>

<sup>1</sup> School of Engineering and Applied Sciences, Harvard University, 29 Oxford Street, Cambridge, MA 02138, USA

<sup>2</sup> Department of Physics, Harvard University, 29 Oxford Street, Cambridge, MA 02138, USA

(Received 10 March 2011; revised 17 August 2011; accepted 22 September 2011)

Controlled gliding during descent has been thought of as a crucial intermediate step toward the evolution of powered flight in a variety of animals. Here we develop and analyse a model for the controlled descent of thin bodies in quiescent fluids. Focusing on motion in two dimensions for simplicity, we formulate the question of steering an elliptical body to a desired landing location with a specific orientation using the framework of optimal control theory with a single control variable. We derive both time- and energy-optimal trajectories using a combination of numerical and analytical approximations. In particular, we find that energy-optimal strategies converge to constant control, while time-optimal strategies converge to bang–coast–bang control that leads to bounding flight, alternating between tumbling and gliding phases. Our study of these optimal strategies thus places natural limits on how they may be implemented in biological and biomimetic systems.

**Key words:** control theory, flow–structure interactions, swimming/flying

---

## 1. Introduction

The origin of flight in insects, birds and mammals is a question of great interest from an evolutionary perspective. Given the relative paucity of fossil evidence, one is thus left grasping for intermediate steps that bridge terrestrial or arboreal locomotion and autonomous flight. Several hypotheses have been proposed for the evolution of wings and controlled flight, and a number of studies (Dudley 2000; Grimaldi & Engel 2005; Bradley *et al.* 2009) have discussed how this might have arisen in a variety of organisms, from dinosaurs to insects. One commonly alluded to pathway for the evolution of active flight posits an intermediate step between simple parachuting and flapping flight, namely controlled aerial descent. Evidence for this in living mammals and reptiles comes from observations of membranes and winglets for controlling descent in these creatures. More recently (Dudley *et al.* 2007; Bradley *et al.* 2009), ant families have been shown to have a surprising gliding ability although their bluff bodies are not particularly suited for streamlined flight. This was first reported in Yanoviak, Dudley & Kaspari (2005) based on the ability of neotropical canopy ants to launch themselves from, glide and eventually land on a tree with an appropriate body orientation. Similar behaviour has been reported in African ants (Yanoviak, Fisher & Alonso 2008), and in bristletails (Yanoviak, Kaspari & Dudley 2009), insects with

† Email address for correspondence: [lm@seas.harvard.edu](mailto:lm@seas.harvard.edu)

very different evolutionary lineage than canopy ants. These observations give some credence to the hypothesis of gliding as an intermediate stage between terrestrial and flying locomotion, see Dudley *et al.* (2007) and Hasenfuss (2008).

However, to give these plausibility arguments substance requires a combination of quantitative experiments and mathematical models that characterize the phase space of stable controllable gliding in the absence of any organs specifically designed for this task. Here, we take a first step in this direction by addressing the question theoretically in a very simple context, inspired by recent biological observations and the relative simplicity of the passive dynamics of a rigid falling object in a quiescent fluid. The latter subject has attracted the curiosity of researchers for more than 150 years due to the intriguing interaction between the motion of the solid and the induced fluid reaction (Lamb 1945), and the small flurry of activity inspired by the regular and irregular motion of a falling card, both from an experimental and theoretical/computational perspective, see for example Mahadevan (1996), Belmonte, Eisenberg & Moses (1998), Mahadevan, Ryu & Aravinthan (1999), Mittal, Seshadri & Udaykumar (2004), Pesavento & Wang (2004) and Andersen, Pesavento & Wang (2005*a,b*). These studies, which focus on both quantitative experiments, and full scale numerical simulations of the governing Navier–Stokes equations, show that a simplified finite-dimensional theory suffices to understand the planar motion of an elliptical cylinder moving in an quiescent fluid, and can capture the qualitative features associated with oscillatory flutter, rotary tumbling motion and transitions between these states. These simplified theories parametrize the drag and vorticity, two quantities that are not present in the classical models that harken back to Kirchhoff, see Lamb (1945), by averaging over the details of the complex vortical motions of the fluid around the body.

Although this minimal parametrization of the drag and vorticity is not adequate for all purposes, the resulting qualitative understanding of the planar dynamics of flutter and tumble in a heavy elliptical cylinder allows us to investigate qualitatively the possibility of controlled descent of such an object by means of a single internal actuator, using the methods of optimal control theory. In § 2 we introduce our model for the physical dynamics of descent and those of a minimal controller subject to some natural constraints. In § 3 we analyse the uncontrolled and controlled dynamics of the body to obtain an estimate of the reachable set. In § 4 we consider the problem of optimal perching that requires the body to reach a particular location with a particular orientation, and we show some examples of trajectories that minimize either the time or the energy used for completing this task. Finally, in § 5 we conclude with some remarks on the biological relevance and efficacy of these strategies and possible future directions.

## 2. Mathematical model

A simple model for the motion of a falling body can be obtained by considering the motion of an infinite elliptical cylinder in an inviscid, incompressible quiescent fluid in a gravitational field. If the cylinder height is much larger than its radius, the resulting motion is essentially two-dimensional with the axis of rotation coinciding with the cylinder's main axis and governed by coupled partial differential equations that link the motion of the surrounding fluid with the dynamics of the solid. As was first shown by Kirchhoff, this is completely equivalent to a reduced order model that can be derived by exploiting the linearity inherent in inviscid fluid dynamics, thus obtaining a finite-dimensional system for the body motion, where the fluid interaction reduces to a

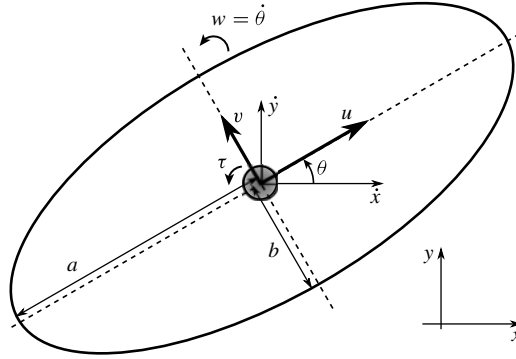


FIGURE 1. Schematic representation of system model. The position of the centre of mass is identified in the laboratory frame  $x$ - $y$ , whereas its orientation is described by the angle  $\theta$  between horizontal direction and major axis. A rotating frame  $u$ - $v$  is attached to the cylinder centre of mass. The control action is represented by a torque  $\tau$ . The system dynamics is reported in (2.1)–(2.6).

renormalization of the mass and inertia tensor, see Lamb (1945). Of course this model for motion in an inviscid fluid misses two crucial ingredients that are important in real motions, associated with viscous drag and vorticity. If these effects can be qualitatively represented in terms of (as yet unknown) forces and torques on the body, we can write the equations of motion for the translating, rotating three-degree-of-freedom body in terms of a moving frame shown in figure 1, as

$$(m + m_1)\dot{u} = (m + m_2)vw - \rho_f \Gamma v - \pi(\rho_s - \rho_f)abg \sin \theta - F, \quad (2.1)$$

$$(m + m_2)\dot{v} = -(m + m_1)uw + \rho_f \Gamma u - \pi(\rho_s - \rho_f)abg \cos \theta - G, \quad (2.2)$$

$$(I + I_a)\dot{w} = (m_1 - m_2)uv + \tau - M, \quad (2.3)$$

$$\dot{x} = u \cos \theta - v \sin \theta, \quad (2.4)$$

$$\dot{y} = u \sin \theta + v \cos \theta, \quad (2.5)$$

$$\dot{\theta} = w. \quad (2.6)$$

Here the state components  $u(t)$  and  $v(t)$  represent the velocities along the main axes of the ellipse,  $w(t)$  the rotational velocity,  $\theta(t)$  the angle of the major axis with the horizontal direction and  $x(t)$  and  $y(t)$  the ellipse's geometrical centre in the laboratory frame,  $m$  is the cylinder mass and  $I$  its moment of inertia,  $m_1$ ,  $m_2$  and  $I_a$  are inertial renormalization terms due to the fluid interaction, and  $\rho_f$  and  $\rho_s$  are, respectively, the fluid and the solid density. For an elliptical cross-section with semi-major axes  $a$  and  $b$  with  $a > b$  the inertial parameters read

$$m = \pi\rho_s ab, \quad I = \frac{1}{4}\pi\rho_s ab(a^2 + b^2), \quad (2.7)$$

$$m_1 = \pi\rho_f b^2, \quad m_2 = \pi\rho_f a^2, \quad I_a = \frac{1}{8}\pi\rho_f(a^2 - b^2)^2. \quad (2.8)$$

To complete the model, we need to describe the circulation around the body  $\Gamma$ , the fluid forces  $F$ ,  $G$ , the fluid torque  $M$  and the control torque  $\tau$ . Attempts to parametrize the effects of aerodynamics forces and torques in the model qualitatively have a long history, but have typically been done in an *ad hoc* way. However, in a series of papers, Wang and coauthors (Pesavento & Wang 2004; Andersen *et al.* 2005a,b) have used simulations and experiments to propose a self-consistent parametric form for these

effects written as

$$\Gamma = -2C_T a \frac{uv}{\sqrt{u^2 + v^2}} + 2C_R a^2 w, \quad (2.9)$$

$$F = \rho_f a \left[ A - B \frac{u^2 - v^2}{u^2 + v^2} \right] \sqrt{u^2 + v^2} u, \quad (2.10)$$

$$G = \rho_f a \left[ A - B \frac{u^2 - v^2}{u^2 + v^2} \right] \sqrt{u^2 + v^2} v, \quad (2.11)$$

$$M = \pi \rho_f a^4 \left[ \frac{V}{L} \mu_\tau + \nu_\tau |w| \right] w, \quad (2.12)$$

where  $C_T$ ,  $C_R$ ,  $A$ ,  $B$ ,  $\mu_\tau$  and  $\nu_\tau$  are non-dimensional constants characterizing the vorticity and drag forces from the surrounding fluid while  $V$  and  $L$  represent, respectively, a characteristic velocity and a characteristic length described later. The quadratic lift and drag terms in the model are consistent with the relatively high Reynolds numbers ( $\sim O(10^3)$ ) associated with ant descent, and can capture the bifurcation between flutter and tumbling as well as the qualitative behaviour of the forces acting on the cylinder during both steady flutter and tumbling. The magnitude of the torque acting on the body is overestimated by this model (Andersen *et al.* 2005b), an effect which shifts the bifurcation threshold for the transition from flutter to tumble. However, since the qualitative behaviours of the true dynamics are captured correctly by this simple low-dimensional model, for our analysis of the question of controlled descent we use expressions (2.9)–(2.12), so that the problem becomes relatively simple and somewhat analytically tractable.

The system dynamics can be conveniently expressed in dimensionless form using the cylinder semi-major axis  $a$  as a characteristic length scale and the velocity  $V = \sqrt{(\rho_s/\rho_f - 1)gb}$ , obtained from the balance between the gravity and a quadratic drag (Mahadevan *et al.* 1999), as a characteristic velocity scale, along with a characteristic force per unit length scale  $\rho_f a V^2$  and a characteristic torque per unit scale  $I_a V^2 a/b$ . This leaves us with the following dimensionless parameters (see Andersen *et al.* 2005a)

$$\beta = \frac{b}{a}, \quad I = \frac{\rho_s b}{\rho_f a}, \quad (2.13)$$

where  $\beta$  represents the cross-section aspect ratio,  $I$  is the non-dimensional moment of inertia. The dynamics can be then written in dimensionless form, with a little abuse of notation by replacing the dimensional variables with their dimensionless versions, as

$$(I + \beta^2)\dot{u} = (I + 1)vw - \Gamma v - \sin \theta - F \quad (2.14)$$

$$(I + 1)\dot{v} = -(I + \beta^2)uw + \Gamma u - \cos \theta - G \quad (2.15)$$

$$\frac{1}{4}[I(1 + \beta^2) + \frac{1}{2}(1 - \beta^2)^2]\dot{w} = (\beta^2 - 1)uv + \tau - M \quad (2.16)$$

$$\dot{x} = u \cos \theta - v \sin \theta \quad (2.17)$$

$$\dot{y} = u \sin \theta + v \cos \theta \quad (2.18)$$

$$\dot{\theta} = w. \quad (2.19)$$

Note that only  $I$  and  $\beta$  appear explicitly in the governing equations. The circulation and the drag terms (2.9)–(2.12) read, in dimensionless form, as

$$\Gamma = \frac{2}{\pi} \left[ -C_T \frac{uv}{\sqrt{u^2 + v^2}} + C_R w \right] \quad (2.20)$$

$$F = \frac{1}{\pi} \left[ A - B \frac{u^2 - v^2}{u^2 + v^2} \right] \sqrt{u^2 + v^2} u \quad (2.21)$$

$$G = \frac{1}{\pi} \left[ A - B \frac{u^2 - v^2}{u^2 + v^2} \right] \sqrt{u^2 + v^2} v \quad (2.22)$$

$$M = [\mu_\tau + \nu_\tau |w|] w. \quad (2.23)$$

For later use, we note that typical values for the dimensionless constants that parametrize the drag and vorticity, as reported in Wang, Birch & Dickinson (2004) and Andersen *et al.* (2005a) are

$$C_T = 1.2, \quad C_R = \pi, \quad A = 1.4, \quad B = 1.0, \quad \mu_\tau = \nu_\tau = 0.2 \quad (2.24)$$

derived for the aerodynamics of thin bodies with Reynolds number around  $10^3$ , the regime associated with ant gliding. In any case, these values do not strongly depend on  $Re$  (Andersen *et al.* 2005a), although  $\mu_\tau$  and  $\nu_\tau$  that are responsible for the rotational time scale increase slightly with decreasing Reynolds number due to an increase in rotational damping.

We finally augment the passive dynamics of the body with an active control action that allows a falling animal to control its orientation and descent velocity. Here, we assume that animals can apply a torque  $\tau$ , for example by bending its body or rotating its legs. This assumption is in accordance with the experimental observations of gliding ants reported in Yanoviak *et al.* (2010) where removal of hind legs results in a severe impairment of control ability, probably because the relatively large length of the legs compared with the body length allows for a large value of  $\tau$ . Although there is a potential shift of the centre of mass because of the motion of the legs, since their mass is small compared with the body mass, here we neglect this effect. We further assume that the rate of change of torque is limited by physiological constraints so that

$$\dot{\tau} = J \quad (2.25)$$

where  $J$ , the angular jerk, is the actual controlled variable with some natural bounds, which we discuss later.

### 3. Reachable set analysis

A first step in analysing the control problem associated with the capability of controlled gliding requires an estimate of the reachable set, i.e. the maximum horizontal range that can be covered given an initial height and some constraints on the maximum power associated with the control action.

The model presented in the previous section exhibits three qualitatively different kinds of motion, namely steady vertical descent, oscillatory flutter and rotary tumbling. Thus, it is convenient to focus the analysis on these three different regimes; the bifurcations between these modes with  $\tau = 0$  have been numerically investigated (Andersen *et al.* 2005a) by varying  $I$  in the limit  $\beta \ll 1$ . For  $I > 3$ , i.e. when the aspect ratio  $b/a$  is at least three times the density ratio  $\rho_f/\rho_s$ , the body flutters and the net horizontal displacement is zero. In the following we limit ourselves to the case where the body passively flutters because it is satisfied by most gliding animals, such as gliding ants and bristletails (Yanoviak *et al.* 2005, 2009). We also note that the alternate case where the system naturally tumbles is much harder to control because a large aspect ratio cylinder induces a strong reaction torque from the fluid that limits the controllability of the system.

To quantify these different regimes, we use a combination of numerical simulations of the complete nonlinear equations (2.14)–(2.19), shown in figure 3, and analytical estimates for the reachable set. To be able to compare our results qualitatively with the observations of ant gliding, we need estimates of the aspect ratio  $\beta$  and the scaled moment of inertia  $I$ . Clearly, the shape of an ant body is not cylindrical; as a first approximation, we assume that it can be represented as an ellipse with a major axis  $a$  equal to the width the body and its extended legs, the body thickness as minor axis  $b$  and an average density  $\rho_s$  obtained by dividing the sum of body mass and mass of the air inside the fitted cylinder by its cross-sectional area. This leads to  $\beta = 0.1$  and  $I = 20$ , which are the parameter values we use in all our simulations of the nonlinear equations (2.14)–(2.19). The results, shown in figure 3 indicate the trends for the position, orientation and velocity of the gliding, tumbling ellipse. To derive analytical estimates for these quantities, we consider separately the two main kinds.

### 3.1. Fixed point motion and fluttering

We start with a consideration of the slow fluttering motion which can be seen as a perturbation of steady descent. Therefore, approximate expressions for vertical and horizontal velocities can be derived by a fixed point analysis. Steady-state conditions are obtained by considering fixed points of (2.14)–(2.16) and (2.19) and lead to

$$0 = (I + 1)vw - \Gamma v - \sin \theta - F, \quad (3.1)$$

$$0 = -(I + \beta^2)uw + \Gamma u - \cos \theta - G, \quad (3.2)$$

$$0 = (\beta^2 - 1)uv + \tau - M, \quad (3.3)$$

$$0 = w. \quad (3.4)$$

In the uncontrolled case, i.e. when  $\tau \equiv 0$ , the last two equations imply  $w = 0$  and  $uv = 0$  so that two subcases can occur:

(a)  $u = 0$ : (3.1) yields  $\sin \theta = 0$ , i.e. the motion is *broadside-on*, and thus

$$v_b^2 \text{sign}(v) = -\frac{\pi \cos \theta}{A + B} \Rightarrow v_b = \begin{cases} \sqrt{\frac{\pi}{A + B}} & \theta = \pi \\ -\sqrt{\frac{\pi}{A + B}} & \theta = 0, \end{cases} \quad (3.5)$$

which follows from (3.2), and corresponds to stable motion.

(b)  $v = 0$ : (3.2) implies  $\cos \theta = 0$ , i.e. the descent is *edge-on*, so that

$$u_e^2 \text{sign}(u) = -\frac{\pi \sin \theta}{A - B} \Rightarrow u_e = \begin{cases} \sqrt{\frac{\pi}{A - B}} & \theta = \frac{3\pi}{2} \\ -\sqrt{\frac{\pi}{A - B}} & \theta = \frac{\pi}{2}, \end{cases} \quad (3.6)$$

which follows from (3.1), where the relation  $A > B$  has been exploited, in accordance with (2.24).

By plugging these relations in (2.17) and (2.18) we estimate the average velocities in the laboratory frame as

$$\langle \dot{x} \rangle = 0 \quad (3.7)$$

$$\langle \dot{y} \rangle = \begin{cases} -\sqrt{\frac{\pi}{A+B}} & \theta = 0, \theta = \pi, \\ -\sqrt{\frac{\pi}{A-B}} & \theta = \frac{\pi}{2}, \theta = \frac{3\pi}{2}. \end{cases} \quad (3.8)$$

These estimates are useful for evaluating, for example, the time of landing given the initial altitude  $y(0)$ . We note that no net horizontal displacement can be achieved with fixed-point motion if  $\tau \equiv 0$ .

For stable broadside-on descent when  $u_b = 0$  and  $v_b = \pm\sqrt{\pi/(A+B)}$ , to estimate the time to achieve steady fluttering we note that the dynamics of the system is greatly simplified because the circulation terms vanish and the drag forces are purely quadratic. Then, (2.15) reduces to

$$(I+1)\dot{v} = -\cos\theta - \frac{1}{\pi}(A+B)v^2\text{sign}(v), \quad (3.9)$$

where  $v > 0$  if  $\theta = \pi$  and  $v < 0$  if  $\theta = 0$ . Focusing on the case  $\theta \simeq 0$  (the case  $\theta \simeq \pi$  can be easily recovered by symmetry), (3.9) admits the analytical solution

$$\tilde{v}(\hat{\tau}) = -\frac{e^{-2\hat{\tau}} - 1}{e^{-2\hat{\tau}} + 1}, \quad (3.10)$$

where

$$\hat{\tau} = (I+1)\sqrt{\frac{\pi}{A+B}}t, \quad \tilde{v} = \frac{v}{v_b}. \quad (3.11)$$

Thus, the time  $T_{ss}$  to reach this steady velocity can be estimated by imposing the condition  $\tilde{v}(\hat{\tau}_{ss}) = (1 - \delta)$ ; when the parameter  $\delta \ll 1$  the time taken is

$$\hat{\tau}_{ss} = -\frac{1}{2} \ln \left( \frac{\delta}{2 - \delta} \right), \quad (3.12)$$

$$\Rightarrow T_{ss} = \frac{I+1}{2} \sqrt{\frac{\pi}{A+B}} \ln \left( \frac{2 - \delta}{\delta} \right). \quad (3.13)$$

We can also find the travelled distance  $y_{ss}$  by integrating (3.9) once more to find

$$y_{ss} = -\frac{\pi}{A+B}(I+1) [\ln(e^{2T_{ss}} + 1) - T_{ss} - \ln 2]. \quad (3.14)$$

When the controller is switched on,  $\tau \neq 0$ , and the position of the fixed points can only be calculated by numerically solving (3.1)–(3.4) due to the nonlinear coupling between them. In figure 2 the location of these fixed points in the state space as a function of  $\tau$  is reported together with the real part of the largest eigenvalue of the dynamics (2.14)–(2.19) linearized around the fixed points. We note that all of the fixed points are linearly unstable, as expected; however, large horizontal velocities can be achieved with this kind of motion, a fact that will be useful in understanding time-optimal trajectories.

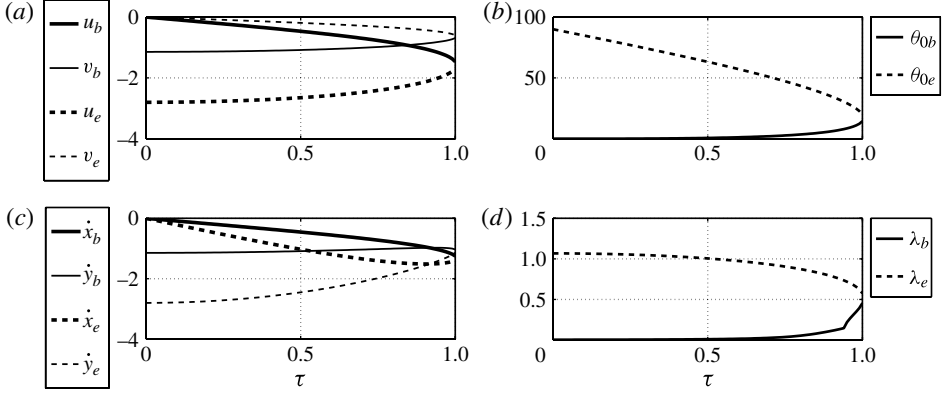


FIGURE 2. Fixed points and linear stability as a function of  $\tau$  showing: (a) velocities in the rotating frame, (b) orientation, (c) velocities in the laboratory frame and (d) real part of the largest eigenvalue of the dynamics (2.14)–(2.19) linearized around the fixed points. The results correspond to the solution of (3.1)–(3.4) with  $\beta = 0.1$ ,  $I = 20$ ,  $C_T = 1.2$ ,  $C_R = \pi$ ,  $A = 1.4$ ,  $B = 1.0$  and  $\mu_\tau = \nu_\tau = 0.2$ . Only positive values of  $\tau$  are displayed; when  $\tau < 0$  they are related to these results via symmetry. The subscripts ‘b’ and ‘e’ indicate, respectively, broadside-on and edge-on motion, as defined in the text.

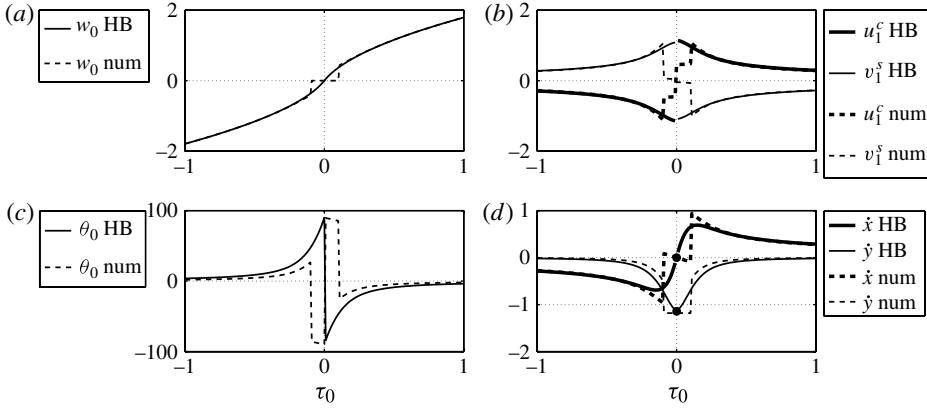


FIGURE 3. Comparison of (a) rotational velocities, (b) velocities in the moving frame, (c) glide angle and (d) velocities in the laboratory frame obtained via the numerical simulation of (2.14)–(2.19) and the HB theory given by (3.34)–(3.40). The circles in the lower right plot represents results of the uncontrolled slowly fluttering mode. The parameters used are  $\beta = 0.1$ ,  $I = 20$ ,  $C_T = 1.2$ ,  $C_R = \pi$ ,  $A = 1.4$ ,  $B = 1.0$  and  $\mu_\tau = \nu_\tau = 0.2$ . We note the good agreement between our analytical estimates and numerical results even fairly close to the transition between fluttering and tumbling, which occurs when  $\tau_0 = 0.1$ .

### 3.2. Tumbling motion

In contrast with the steady descent just described, the additional degree of freedom provided by the torque  $\tau$  can be used to induce tumbling motion, where rotational lift and drag forces are exploited to obtain net horizontal displacement with greater efficiency, robustness and stability.

In the limit of rapid tumbling, a simplified analysis can be carried out by averaging over the fast oscillations in the system dynamics. Considering only the first harmonic



of  $u$ ,  $v$  and  $\theta$ , we assume that

$$u \simeq u_0 + u_1^c \cos(\Omega^u t) + u_1^s \sin(\Omega^u t), \quad (3.15)$$

$$v \simeq v_0 + v_1^c \cos(\Omega^v t) + v_1^s \sin(\Omega^v t), \quad (3.16)$$

$$w \simeq w_0 + w_1^c \cos(\Omega^w t) + w_1^s \sin(\Omega^w t), \quad (3.17)$$

$$\theta \simeq \theta_0 + w_0 t + \frac{w_1^c}{\Omega^w} \sin(\Omega^u t) - \frac{w_1^s}{\Omega^w} \cos(\Omega^w t). \quad (3.18)$$

On using these approximations in the differential equations (2.14)–(2.19), at leading order we are left with an algebraic system of equations in the 13 unknowns

$$[u_0, u_1^c, u_1^s, \Omega^u, v_0, v_1^c, v_1^s, \Omega^v, w_0, w_1^c, w_1^s, \Omega^w, \theta_0] \quad (3.19)$$

for which an exact solution seems unlikely. However, geometry and symmetry considerations allow for further simplification. First, the oscillation frequencies are not independent because the symmetry of the system imposes the following relations

$$\Omega^u = \Omega^v = w_0, \quad \Omega^w = 2\Omega^u \quad (3.20)$$

so that only one of them needs to be evaluated. In addition, by noting that the dynamics is time-invariant, the time axis can be chosen such that one of the coefficients  $u_1^c$ ,  $u_1^s$ ,  $v_1^c$ ,  $v_1^s$  vanishes and, therefore,  $u_1^s = 0$  can be set to zero. In the fast tumbling limit,  $w_0 > \sqrt{w_1^{c2} + w_1^{s2}}$  so that  $w$  and  $\theta$  read

$$w \simeq w_0, \quad (3.21)$$

$$\theta \simeq \theta_0 + w_0 t. \quad (3.22)$$

This latter hypothesis is valid only far from the bifurcation threshold that separates the fluttering and tumbling phases; indeed, the validity (or not) of this assumption represents the main source of error in the following results. Finally, noting, as in Andersen *et al.* (2005b), that during tumbling motion the rotational term in the circulation (2.20) is dominant, we neglect the translational contribution to the circulation in our approximate analysis.

Using the approximate relations (3.15)–(3.16) and (3.21)–(3.22) in the dynamical equations (2.14)–(2.16) and balancing the average and the first harmonic terms yields the following system of algebraic equations

$$(I + 1)w_0 u_0 - \frac{2}{\pi} C_R w_0 v_0 - F_0 = 0, \quad (3.23)$$

$$(I + \beta^2)w_0 u_1^c + (I + 1)w_0 v_1^s - \frac{2}{\pi} C_R w_0 v_1^s - \cos \theta_0 - F_1^s = 0, \quad (3.24)$$

$$(I + 1)w_0 v_1^c - \frac{2}{\pi} C_R w_0 v_1^c - \sin \theta_0 - F_1^c = 0, \quad (3.25)$$

$$-(I + \beta^2)w_0 u_0 + \frac{2}{\pi} C_R w_0 u_0 - G_0 = 0, \quad (3.26)$$

$$(I + 1)w_0 v_1^c + \sin \theta_0 - G_1^s = 0, \quad (3.27)$$

$$-(I + 1)w_0 v_1^s - (I + \beta^2)w_0 u_1^c + \frac{2}{\pi} C_R w_0 u_1^c - \cos \theta_0 - G_1^c = 0, \quad (3.28)$$

$$(\beta^2 - 1) \frac{u_1^c v_1^c}{2} + \tau_0 - \mu_\tau w_0 - \nu_\tau w_0^2 \text{sign}(w_0) = 0, \quad (3.29)$$

where the nonlinearities in the drag forces and torque (2.21)–(2.23) have been approximated by the first terms of the respective Fourier's expansions, i.e.

$$F \simeq F_0 + F_1^c \cos(w_0 t) + F_1^s \sin(w_0 t), \quad (3.30)$$

$$G \simeq G_0 + G_1^c \cos(w_0 t) + G_1^s \sin(w_0 t), \quad (3.31)$$

$$M \simeq M_0 + F_1^c \cos(w_0 t) + F_1^s \sin(w_0 t). \quad (3.32)$$

The presence of the average torque  $\tau_0$  in (3.29) suggests the use of a constant control torque since oscillations in it will not have effect on  $w_0 = \langle w \rangle$ . While this may not always be viable, in ants for example, it is certainly plausible in bristletails or in artificial systems. To evaluate how other forms of the torque  $\tau$  influences the system dynamics, we also analysed the response to an impulsive periodic torque of varying maximum amplitude, period and impulse duration (see appendix A). Again, only the average value is relevant for the dynamics, with all higher harmonic effects having a very small influence (see appendix A). In light of this, from now on, we assume that torque is constant, with

$$\tau = \tau_0, \quad (3.33)$$

noting that it actually represents the average torque. Then, the dynamics of torque actuation (2.25) can be completely neglected since  $J(t) = 0$  throughout the trajectory.

As suggested by our numerical simulations (3.23) and (3.26) can be easily satisfied by imposing  $u_0 = v_0 = 0$ . Then, the remaining equations can be solved in a self-consistent manner if we consider the phase shift of  $\pi/2$  between  $u$  and  $v$  given by geometrical constraints. In this case,  $u_1^c = 0$  implies  $v_1^c = 0$  too, (3.29) decouples from the other equations, and an estimate of the average angular velocity follows from (3.29) as

$$w_0 = \frac{\mu_\tau \pm \sqrt{\mu_\tau^2 + 4\tau_0 v_\tau \text{sign}(w_0)}}{-2v_\tau \text{sign}(w_0)} = \begin{cases} \frac{\mu_\tau - \sqrt{\mu_\tau^2 + 4\tau_0 v_\tau}}{-2v_\tau} & (> 0) \quad \tau > 0 \\ \frac{\mu_\tau - \sqrt{\mu_\tau^2 - 4\tau_0 v_\tau}}{2v_\tau} & (< 0) \quad \tau < 0. \end{cases} \quad (3.34)$$

Moreover, if the aspect ratio  $\beta \gg \rho_f/\rho_s$  then  $I \gg 1$  while  $C_R/\pi \sim O(1)$  so that (3.24), or equivalently (3.28), gives at leading order

$$(1 + \beta^2) u_1^c = -(I + 1) v_1^s \quad \Rightarrow \quad u_1^c = -\frac{I + 1}{I + \beta^2} v_1^s = \kappa v_1^s, \quad (3.35)$$

while the remaining terms provide

$$-\frac{2}{\pi} C_R w_0 v_1^s - \cos \theta_0 = 0 \quad \Rightarrow \quad v_1^s = -\frac{\pi \cos \theta_0}{2C_R w_0}. \quad (3.36)$$

Note that this latter relation corresponds to the situation in which most of the weight is supported by the rotational lift, while (3.35) implies that the oscillation in  $u$  and  $v$  velocities are only due to the rotating frame. The only remaining unknown is  $\theta_0$ . An estimate for this quantity can be derived from (3.25), or equivalently from (3.27), by approximating the term  $F_1^c$  so that (3.25) reduces to a second-order equation in the

unknown  $\sin \theta_0$  (see appendix B). Thus,  $\theta_0$  can be derived as

$$\theta_0 = \begin{cases} \sin^{-1} \left[ \frac{-1 + \sqrt{1 + 4\Theta^2}}{-2\Theta} \right] & (< 0) \quad w_0 > 0, \\ \sin^{-1} \left[ \frac{-1 + \sqrt{1 + 4\Theta^2}}{2\Theta} \right] & (> 0) \quad w_0 < 0, \end{cases} \quad (3.37)$$

where

$$\Theta = \left[ -A \left( \frac{5}{8} + \frac{3}{8}\kappa^2 \right) + B \left( -\frac{3}{16} + \frac{11}{16}\kappa^4 \right) \right] \frac{\kappa \pi^2}{4C_R^2 w_0^2} \quad (> 0). \quad (3.38)$$

Using the relations (3.37) and (3.34) the desired quantities  $\theta_0$  and  $w_0$  can be estimated and substituted in (3.36) and (3.35); this allows us to solve the algebraic system (3.23)–(3.29) derived from harmonic balance (HB).

Finally, given  $u_1^c$ ,  $v_1^s$  and  $\theta_0$  we can estimate the reachable set for tumbling motion. In fact, from (2.17)–(2.18) we estimate the average horizontal and vertical velocities as

$$\langle \dot{x} \rangle = \langle u \cos \theta - v \sin \theta \rangle = \frac{u_1^c}{2} \cos \theta_0 - \frac{v_1^s}{2} \cos \theta_0, \quad (3.39)$$

$$\langle \dot{y} \rangle = \langle u \sin \theta + v \cos \theta \rangle = \frac{u_1^c}{2} \sin \theta_0 - \frac{v_1^s}{2} \sin \theta_0. \quad (3.40)$$

In figure 3, we show a comparison between the predictions of the harmonic balance theory (3.34)–(3.40) and numerical simulations of the full equations (2.14)–(2.19). We note that, as expected, when  $\tau_0$  is large, and thus  $w_0$  is sufficiently large, the approximate solutions given by the harmonic balance match the full model results very accurately.

Having analysed the reachable set for the two steady regimes, we now turn to the transition between flutter and tumble. In this regime the model is likely to be less accurate; furthermore the harmonic balance method fails for small values of  $\tau_0$  because the relation between the angular frequencies is  $\Omega^u = \Omega^w = (1/2)\Omega^v$  instead of (3.20) and moreover the condition  $w_0 > \sqrt{w_1^{c2} + w_1^{s2}}$  is clearly not satisfied because  $w_0 = 0$ . In the ‘slow tumbling’ regime, i.e. just above the critical value of  $\tau$ , the state variables present significant harmonic distortion with respect to the pure sinusoidal behaviour, see for example figure 4 for a comparison between  $u$  and  $v$  in the ‘slow’ and ‘fast’ tumbling regime. This introduces additional errors in the harmonic balance because in (3.15)–(3.18) we completely neglect contributions from higher harmonics.

Nevertheless, the estimates for the falling body translational velocities (3.39)–(3.40) allow for an estimate of the reachable set based on first harmonic effects that neglects transients. Then, given an initial position  $(x_0, y_0)$  in the laboratory frame, the maximum reachable distance can be estimated by the following two steps procedure:

- (a) find the value of the torque that provides the maximum ratio between horizontal and vertical velocity, i.e.

$$\hat{\tau}_0 = \arg \max_{|\tau_0| \leq \tau_{max}} \frac{\langle \dot{x} \rangle}{\langle \dot{y} \rangle} \quad (3.41)$$

and denote by  $\widehat{\langle \dot{x} \rangle}$  and  $\widehat{\langle \dot{y} \rangle}$  the corresponding velocities;

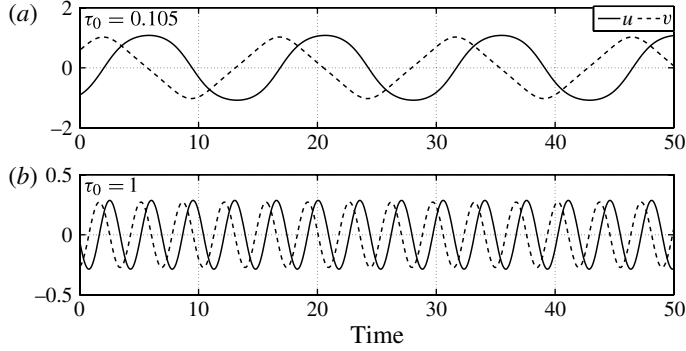


FIGURE 4. Comparison of the velocity components  $u, v$  in the (a) slow and (b) fast tumbling regimes obtained using numerical simulations of (2.14)–(2.19). The parameters used are  $\beta = 0.1$ ,  $I = 20$ ,  $C_T = 1.2$ ,  $C_R = \pi$ ,  $A = 1.4$ ,  $B = 1.0$  and  $\mu_\tau = \nu_\tau = 0.2$ . Note the larger harmonic distortion of the quantities in the slow tumbling regime.

(b) estimate the maximum horizontal distance that can be covered as

$$\Delta x_{max} = x_0 \pm \frac{y_0}{\langle \dot{y} \rangle} \langle \hat{x} \rangle. \quad (3.42)$$

These results can be exploited for designing a control law capable of steering the system from its initial position to a given final position, by designing a two-phase strategy where the body first tumbles and then switches to fluttering motion. The time spent in the tumbling phase can be estimated by (3.39) by  $T_{tumble} = (x_f - x_0)/\langle \dot{x} \rangle$  after which the system is forced to switch to fluttering with no average horizontal velocity. We observe that the control law is not unique but characterized by a family parametrized by the value of  $\tau_0$  used during the tumbling phase. In this approximation, the landing position is thus also controlled only approximately because all of the transient phases have been neglected. However, these problems can be overcome by using optimal control techniques to obtain a unique control law capable of exactly steering the system to a desired final configuration.

#### 4. Optimal control for landing and perching

The approximate control design described in the previous section assumes steady-state estimates without imposing any condition on the final orientation. Thus, it is not very useful for perching problems where the orientation at landing is crucial. Furthermore, since no optimality criterion was considered, there is no unique solution for the problem of descent. To overcome these problems we consider the perching task in the framework of optimal control theory. We note that due to the lack of complete controllability, i.e. not all of the values of the state vector  $[x, y, \theta, u, v, w]$  can be reached from any initial condition, we cannot impose arbitrary constraints on the final position and orientation. However, using the results from §3 we can obtain estimates of the reachable set, and thus avoid imposing unattainable final conditions. Our optimal trajectories are determined under the implicit assumption of open-loop control, where no feedback from sensory information is used to dynamically compensate for disturbances and potential model mismatch due, for example, to the presence of wind. This raises the important question about how it is possible to implement such strategies in closed-loop form. Unfortunately, the search space for

closed-loop optimal control strategies in high dimensions, as here, is so large that we are unable to get any useful analytical results to validate the numerics. From a biological perspective, we do not know exactly what quantities an animal is capable of measuring during gliding, and the noise in such measurements, and therefore any model would require *ad hoc* hypotheses. For these reasons we limit our analyses to open-loop optimal strategies.

To formulate the optimal control problem we define a performance index that has to be minimized along optimal trajectories. Two commonly used performance indexes are the total time necessary to reach the final position and the total energy spent for the control action. This allows us to define a performance index  $\mathcal{C}$  as

$$\mathcal{C} = \int_0^T [1 + \eta(\tau^2 + \alpha J^2)] dt = T + \eta \int_0^T (\tau^2 + \alpha J^2) dt, \quad (4.1)$$

where  $\tau^2$  is a proxy for the instantaneous input power and  $\eta > 0$  represents the relative weight between energy-optimality and time-optimality. We note that the rigorous expression for the input power is  $\tau \cdot w$ . Since the quadratic drag law in (2.16) and (2.23) implies that the average value of  $w$  scales as  $w \sim \tau^{1/2}$ , we have  $\tau \cdot w \sim \tau^{3/2}$ . We choose the form  $\tau^2$  with a stronger dependence mainly because it allows for simpler calculations. As  $\eta \rightarrow 0$  the problem reduces to time-optimal control, while as  $\eta \rightarrow \infty$  the total energy is minimized. A weight  $\alpha$  is included to account for eventual costs associated with the control action  $J$ , but as discussed later it will not have a great impact on the structure of the optimal trajectories. Here, we let the final time  $T$  be free; it will be determined as part of the problem solution. Formally, the optimal perching problem can be stated as

$$\min_J \mathcal{C} = \min_J \int_0^T [1 + \eta(\tau^2 + \alpha J^2)] dt \quad (4.2)$$

$$\dot{X} = G_0(X) + G_1 J \quad (4.3)$$

$$X(0) = X_0 \quad (4.4)$$

$$X(T) \in \mathcal{F} \quad (4.5)$$

$$\mathcal{F} = \{X(T) \in \mathbb{R}^7 : x(T) = x_f, y(T) = y_f, \theta(T) = \theta_f \pmod{2\pi}, \\ |\dot{x}(T)| \leq \dot{x}_{\max}, |\dot{y}(T)| \leq \dot{y}_{\max}, |w(T)| \leq w_{\max}\} \quad (4.6)$$

$$|\tau| \leq \tau_{\max} \quad (4.7)$$

$$|J| \leq J_{\max}, \quad (4.8)$$

where  $X = [u, v, w, x, y, \theta, \tau]$  is the (extended) state of the system and (4.3) is a concise way of writing the system dynamics (2.14)–(2.19) together with the torque dynamics (2.25) (see appendix C). The set of desired final configurations is defined by  $\mathcal{F}$ . We note that the final position and orientation are strictly enforced, whereas only upper bounds on the magnitude of final velocities are included. Furthermore, both the applied torque  $\tau$  and its derivative  $J$  have to satisfy magnitude constraints along the whole trajectory.

Necessary conditions that have to be satisfied by optimal trajectories are given by the Pontryagin maximum principle, see for example Pontryagin *et al.* (1962) and Kirk (2004) for a description of these conditions. However, the high dimension of the state space of the system, together with its nonlinear nature, does not allow for the analytical description of optimal trajectories and therefore solutions must be obtained by means of numerical algorithms. These problems become even worse since

algorithms for finding a trajectory that satisfies the necessary conditions can also suffer from the curse of (high) dimensionality of the system, so that the computational time can easily be so large that the problem is intractable in practice if good guesses are not available. To overcome these problems we use the following three-step procedure:

- (a) start with the approximate solution of § 3 to find a good initial guess for the optimal trajectory;
- (b) use these to find trajectories that satisfy optimality conditions at least at a finite number of points using a numerical algorithm;
- (c) check the quality of the resulting trajectories analytically using the necessary optimality conditions provided by the Pontryagin maximum principle.

The trajectory used as an initial guess is composed of two phases, a tumbling phase and a fluttering phase, based on the reachable set estimates in § 3. Then the control action for the initial guess is defined as in (3.33) for the tumbling phase and the determination of the exact form of  $J$  (and consequently  $\tau$ ) is carried out numerically in the second step of the procedure, as described in the following.

We first consider an energy-optimal trajectory, for which the performance index can be written as

$$U = \frac{\mathcal{E}}{\eta} = \int_0^T (\tau^2 + \alpha J^2) dt \simeq \int_0^{T_{on}} \tau_0^2 dt = \tau_0^2 T_{on}, \quad (4.9)$$

where  $T_{on}$  represents the total duration of the tumbling phase, during which time the control is active, and all of the transients have been neglected. Here the jerk  $J$  does not enter in the calculations because  $\tau = \tau_0 = \text{constant}$  implies  $J = 0$  except during the transients. From the reachable set analysis of § 3 one obtains

$$\arg \min_{\tau_0} U \simeq \arg \min_{\tau_0} \tau_0^2 T_{on} \simeq \arg \min_{\tau_0} \tau_0^2 \frac{x_f}{\langle \dot{x} \rangle} \simeq \arg \min_{\tau_0} \frac{\tau_0^2}{\langle \dot{x} \rangle}, \quad (4.10)$$

where  $\tau_0$  and  $\langle \dot{x} \rangle$  are related as shown in figure 3. In figure 5, we show  $\tau_0^2 / \langle \dot{x} \rangle$  as a function of  $\tau_0$ , and see that a good initial guess for energy-optimal trajectories can be obtained by choosing the smallest value of  $\tau_0$  that allows the body to land at the desired final position. We can explain the qualitative behaviour of  $U$  as a function of  $\tau_0$  by noting that when  $\tau_0 \gg \mu_\tau^2 / 4\nu_\tau = 0.05$  (3.34) implies  $w_0 \simeq -(\mu_\tau / 2\nu_\tau) + \sqrt{\tau_0 / \nu_\tau} \sim \sqrt{\tau_0}$  and, therefore, by plugging (3.36) and (3.39) in (4.10), we obtain

$$U \simeq \tau_0^2 \frac{2C_R w_0}{\pi \cos^2 \theta_0} \sim \tau_0^{5/2} \quad (4.11)$$

or, in dimensional units,

$$U \simeq \tau_0^{5/2} \frac{2\rho_f C_R x_f}{\pi (\rho_s - \rho_f) abg \cos^2 \theta_0 \sqrt{\pi \rho_f \nu_\tau}}, \quad (4.12)$$

where we have used  $\cos^2 \theta_0 \simeq 1$  because  $\theta_0$  quickly converges to values close to zero, see figure 3. We also note that if the rigorous expression for input power were used in (4.1) then (4.11) would read  $U \sim \tau_0^2$  and the qualitative behaviour reported in figure 3 is preserved. Finally, the minimum torque that allows the body to land at the desired location is given by the implicit relation

$$\tan \theta_0(\tau_0) \leq \frac{y_f}{x_f} \quad (4.13)$$

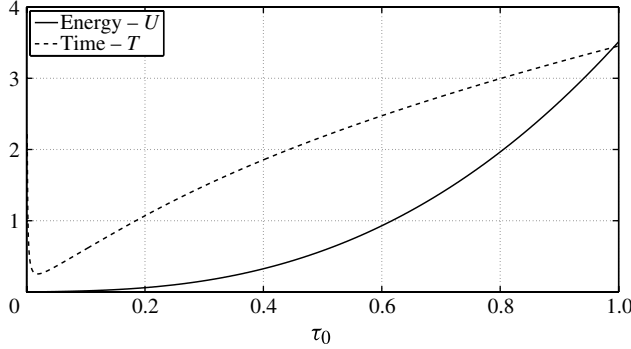


FIGURE 5. The energy  $U$  for energy-optimal trajectories as given by (4.10) and the time  $T$  for time-optimal trajectories estimates as given by (4.14) as a function of the control torque  $\tau_0$ . Parameter choices are  $\beta = 0.1$ ,  $I = 20$ ,  $C_T = 1.2$ ,  $C_R = \pi$ ,  $A = 1.4$ ,  $B = 1.0$  and  $\mu_\tau = \nu_\tau = 0.2$ . We note the presence of a distinct minimum for  $T$  and none for  $U$ .

obtained by imposing  $y_f \geq \langle \dot{y} \rangle T_{on}$  with  $T_{on} = x_f / \langle \dot{x} \rangle$  and  $\langle \dot{x} \rangle$ ,  $\langle \dot{y} \rangle$  as in (3.39)–(3.40).

By following a similar procedure a good guess for time-optimal trajectories can also be obtained. In fact, let us now consider a trajectory composed by an initial tumbling phase of duration  $T_t$  followed by a fluttering phase of duration  $T_f$ . In such a situation

$$\begin{aligned} \mathcal{C} = T_t + T_f &\simeq T_t + \frac{y_f - y(T_t)}{\langle \dot{y}_{flutter} \rangle} \simeq T_t + \frac{y_f - T_t \langle \dot{y}_{tumble} \rangle}{\langle \dot{y}_{flutter} \rangle} \\ &\simeq T_t \left( 1 - \frac{\langle \dot{y}_{tumble} \rangle}{\langle \dot{y}_{flutter} \rangle} \right) + \frac{y_f}{\langle \dot{y}_{flutter} \rangle} \simeq \left( 1 - \frac{\langle \dot{y}_{tumble} \rangle}{\langle \dot{y}_{flutter} \rangle} \right) \frac{x_f}{\langle \dot{x}_{tumble} \rangle} + \frac{y_f}{\langle \dot{y}_{flutter} \rangle}, \end{aligned} \quad (4.14)$$

where the approximations  $y(T_t) \simeq T_t \langle \dot{y}_{tumble} \rangle$  and  $T_t \simeq x_f / \langle \dot{x}_{tumble} \rangle$  have been introduced. Figure 5 shows the total time  $T$  as a function of  $\tau_0$ ; it is evident that a good initial guess will be a trajectory with the smallest  $\tau_0$ , without exceeding the minimum  $\tau \simeq 0.02$ . Again, we can obtain an approximate solution for  $T$  as a function of  $\tau_0$  by noting that the last term in (4.14) does not depend on  $\tau_0$  and that the remaining expression can be rewritten as

$$T \simeq \frac{1}{\langle \dot{x}_{tumble} \rangle} - \frac{\langle \dot{y}_{tumble} \rangle}{\langle \dot{x}_{tumble} \rangle \langle \dot{y}_{flutter} \rangle} \simeq \frac{2C_R w_0}{\pi \cos^2 \theta_0} - \frac{\tan \theta_0}{\langle \dot{y}_{flutter} \rangle} \quad (4.15)$$

or, in dimensional units,

$$T \simeq \frac{2\rho_f C_R x_f w_0}{\pi (\rho_s - \rho_f) abg \cos^2 \theta_0} - \frac{x_f \tan \theta_0}{\langle \dot{y}_{flutter} \rangle}. \quad (4.16)$$

Far from  $\tau_0 = 0$ , where the second term is negligible and  $\cos^2 \theta_0 \simeq 1$ , we still have  $T \sim \sqrt{\tau_0}$  as in the energy-optimal case, but as  $\tau_0$  goes to zero, the first term diverges faster than the second term and the total time goes to infinity as  $T \sim 1/\tau_0$ . According to this analysis a global minimum is then always expected, regardless of the actual choice of the parameter values. Moreover, the position of such minimum must lie in a neighbourhood of the crossover value  $\tau = \mu_\tau^2 / 4\nu_\tau \simeq 0.05$  that separates the regions of validity of the approximations  $w_0 \sim \sqrt{\tau_0}$  and  $w_0 \sim 1/\tau_0$ .

To summarize, in the process of building good initial guesses, we neglect all information about final orientation and terminal velocities defined in (4.6). In the



second step these constraints are taken into account and thus the resulting trajectory approximations will satisfy all of the conditions in (4.2)–(4.8), at least at a finite number of points. All our numerical results have been obtained using the GPOPS package that implements a direct pseudospectral transcription method to solve optimal control problems. In particular, the optimal control problem is converted into a finite-dimensional optimization problem by discretizing time into a finite subset of points and solving the problem only on this subset. The number  $N$  of mesh point is chosen so that the solution satisfies the necessary optimality conditions with good accuracy (see appendix C). The resulting optimization problem is then solved by the sequential quadratic programming solver SNOPT described in Gill, Murray & Saunders (2005) to obtain an approximate optimal trajectory. For a detailed description of the algorithm implemented in GPOPS please refer to Benson (2004), Benson *et al.* (2006), Huntington (2007), Huntington & Rao (2008), Huntington, Benson & Rao (2007a) and Huntington *et al.* (2007b), Garg *et al.* (2010) and Rao *et al.* (2010). The local nature of the optimization algorithm requires a good guess to skip local minima and numerical problems and therefore the guesses obtained by the just described procedure will be used for this purpose. A multistart optimization procedure was performed on a restricted set of trajectories to confirm that the guesses obtained via harmonic balance actually lead to the global minimum. An accuracy check for these trajectories via comparison with the analytically necessary optimality conditions is reported in appendix C.

Assuming that the body starts out at rest, we consider optimal control problems where the initial state  $X_0 = [00000000]$ , and the final state is defined by  $x_f = 100$ ,  $y_f = -50$ ,  $\theta_f = 45^\circ$ , along with constraints on the dimensionless maximum torque and the rate of change of torque  $\tau_{max} = 1$ ,  $J_{max} = 1$  to calculate representative time- and energy-optimal trajectories. In this setting the trajectory starts with the object having zero velocity and the control torque is turned on immediately, when drag and lift forces are still very small. An alternative strategy would be to delay the activation of the controller until the vertical velocity reaches the steady-state value, to exploit the effects of finite drag and lift. However, the performance losses associated with the time to reach the state and the energy needed to switch from steady fluttering to tumbling make the first strategy favourable. Although the fine details of the trajectories clearly depend on the chosen values of the control constraint parameters, the qualitative structure of the trajectories is robust with respect to variations of  $\tau_{max}$  and  $J_{max}$  in the range  $\tau_{max} \in [.5, 2]$  and  $J_{max} \in [0.1, 10]$ .

The energy-optimal trajectory is reported in figure 6(a,b), whereas the time-optimal trajectory is plotted in figure 7(a,b). In both cases no bounds on final velocities were imposed, i.e.  $\dot{x}_{max} = \dot{y}_{max} = w_{max} \rightarrow +\infty$  in (4.6). We assess the (local) optimality of these trajectories by comparing them with the necessary conditions for optimality given by the Pontryagin maximum principle (see appendix C).

Energy-optimal strategies consist of using the minimum, almost constant, torque capable of generating enough lift to reach the desired final position, as expected. On the other hand, as usual in time-optimal control problems, time-optimal trajectories are of ‘bang–coast–bang’ type, i.e. the control switches to one of its bounds until the path constraint become active and it is zero on constrained arcs. Moreover, we see that a weight  $\alpha \neq 0$  does not change the structure of the energy-optimal trajectory a lot because  $J \simeq 0$  almost everywhere.

It is worth noting that the time-optimal trajectory is composed of a succession of tumbling and gliding phases that correspond, respectively, to active lift generation and passive gliding. This behaviour is reminiscent of bounding flight strategies proposed



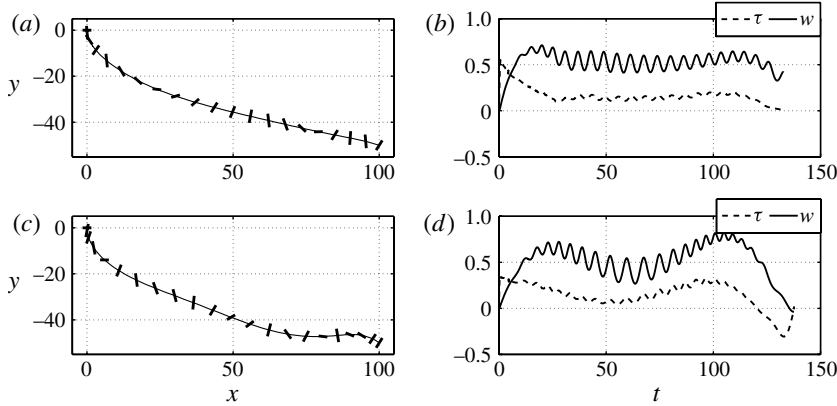


FIGURE 6. (a) Energy-optimal trajectory of the body without bounds on final velocities ( $\dot{x}_{max} = \dot{y}_{max} = w_{max} \rightarrow +\infty$ ), also showing the orientation of the body. (b) Optimal torque  $\tau$  and the angular velocity  $w$ . Note the oscillatory form of the torque with a non-zero mean  $\langle \tau \rangle \simeq 0.13$  (HB prediction  $\tau_0 = 0.19$ ). (c) Energy-optimal trajectory with bounds on final velocities  $\dot{x}_{max} = \dot{y}_{max} = w_{max} = 0.5$  also showing the orientation of the body. (d) Optimal torque  $\tau$  and the angular velocity  $w$ . We note that the final velocity constraints satisfaction induces a lift loss at the very end of the trajectory and therefore the torque  $\tau$  presents a secondary peak to compensate that loss. All simulations used the parameter values  $\beta = 0.1$ ,  $I = 20$ ,  $C_T = 1.2$ ,  $C_R = \pi$ ,  $A = 1.4$ ,  $B = 1.0$  and  $\mu_\tau = \nu_\tau = 0.2$ . The relative location and orientation of the ‘perch’ are  $x_f = 100$ ,  $y_f = -50$ ,  $\theta_0 = 45^\circ$  and the constraints on the control variables are set to  $\tau_{max} = 1$  and  $J_{max} = 1$ .

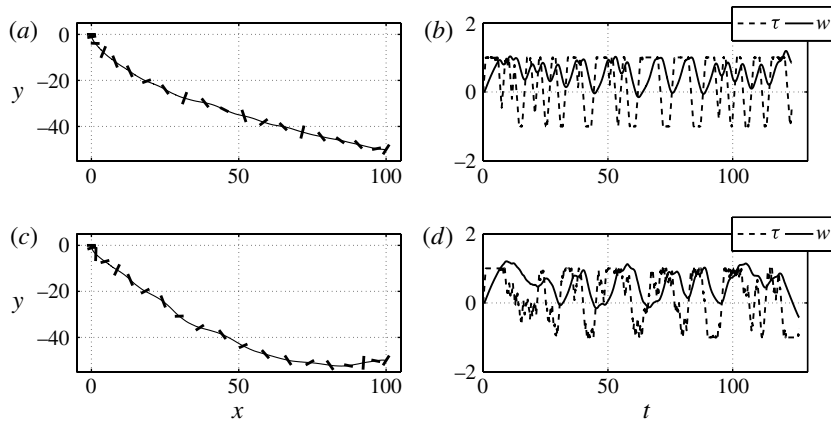


FIGURE 7. (a) Time-optimal trajectory without bounds on final velocities ( $\dot{x}_{max} = \dot{y}_{max} = w_{max} \rightarrow +\infty$ ) also showing the orientation of the body. (b) Optimal torque  $\tau$  and the angular velocity  $w$ . We note that the torque is bang-coast-bang with a non-zero mean  $\langle \tau \rangle = 0.26$  (HB prediction  $\tau_0 = 0.19$ ). (c) Time-optimal trajectory with bounds on final velocities  $\dot{x}_{max} = \dot{y}_{max} = w_{max} = 0.5$  also showing the orientation of the body. (d) Optimal torque  $\tau$  and the angular velocity  $w$ . All simulations used the parameter values  $\beta = 0.1$ ,  $I = 20$ ,  $C_T = 1.2$ ,  $C_R = \pi$ ,  $A = 1.4$ ,  $B = 1.0$  and  $\mu_\tau = \nu_\tau = 0.2$ . The relative location and orientation of the ‘perch’ are  $x_f = 100$ ,  $y_f = -50$ ,  $\theta_0 = 45^\circ$  and the constraints on the control variables are set to  $\tau_{max} = 1$  and  $J_{max} = 1$ .

in Rayner (1985) and Tobalske (2010) as a mean to optimize energy in small birds, but we observe it here in the opposite extreme, where the energy does not enter in the performance index at all. We can qualitatively explain this behaviour by looking at the location of the fixed points reported in figure 2; all gliding phases occur in the proximity of the orientation  $\theta$  corresponding to the steady-state motion with  $\tau \simeq 1$  and this observation suggests that the time-optimal trajectory exploits the high horizontal velocity of this (unstable) steady motion, but during this phase the system loses lift, so that this must eventually be recovered by temporarily inducing tumbling. Such strategy then allows combining the large horizontal velocities typical of steady angle gliding to the small vertical velocities achieved during tumbling.

When there are bounds on the final velocities, such that  $\dot{x}_{\max} = \dot{y}_{\max} = w_{\max} = 0.5$ , the energy- and time-optimal trajectories are shown in figures 6(c,d) and 7(c,d). We note that the overall structure of the solution is preserved and the optimal control strategy is affected only in a ‘boundary’ layer at the end of the trajectory.

## 5. Discussion

We have analysed a simple planar model for the controlled descent of a thin solid body subjected to gravity in a quiescent fluid, inspired by the behaviour of gliding canopy and African ants and bristletails, and gained insight on strategies perching optimally. In particular, by exploiting harmonic balance techniques we first obtained an analytical estimate of the reachable set from a given initial height. We then solved the problem of optimal perching in the framework of optimal control theory and determined trajectories that minimize either the time or the energy for reaching a desired position and orientation. Although the underlying model average over the complex vortical fluid dynamics associated with falling bodies, our results should nevertheless provide a qualitative guide to the phenomena at play.

Our minimal theoretical results based on harmonic balance analysis complement the results obtained using numerical optimal control and show that tumbling motion and rotational lift can be successfully exploited to control the descent of the body and achieve smaller glide angles than simple gliding via fixed point motion associated with simple flutter or tumble, where we have defined the glide angle as the ratio between vertical and horizontal velocities. Interestingly, with some reasonable bounds on the maximum torque  $|\tau| \leq \tau_{\max} = \pi(\rho_s - \rho_f)a^2bg$ , corresponding to shifting the centre of mass to the extremities of the body, further from the geometric centre, we show that it is possible to achieve very shallow glide angles of about  $\theta_0 \simeq 10^\circ$ , which are far better than those seen in canopy ants ( $\theta_0 \simeq 75^\circ$  as in Yanoviak *et al.* 2009), or sugar gliders ( $\theta_0 \simeq 29^\circ$  as in Jackson 2000) and close to a recently designed artificial glider ( $\theta_0 \simeq 15^\circ$  as in Cory & Tedrake 2008).

Furthermore, we see that it is possible to determine an energy-optimal control strategy that follows by using the smallest constant value of the torque allowable to reach the final target. Our results also show that minimum time trajectories exploit unsteady effects to combine large horizontal velocities and relatively small vertical velocities and resemble bounding flight; perhaps they ought to be termed ‘bounding gliding’. In a biological context, these two optimal strategies may characterize the limits of performance that the animal is limited by; for example, time-optimality may be better suited for escape while energy-optimality may be better suited for foraging. Our results also suggest the use of steady tumbling motion for artificial glider systems, as alternatives to the classical approach based on fixed point motion stabilization as, for example, in Woolsey & Leonard (2002) and Roberts, Cory & Tedrake (2009). This is borne out by both the fact that insects have pursued such strategies for hundreds of

millions of years and our study that shows that it may be possible to increase flight performance using rotational lift.

From the perspective of the evolution of flight, our study shows that fairly simple controllers with reasonable constraints can lead to effective, efficient controlled gliding descent. An important quantitative question that our study raises is the role of body morphology and neural dynamics that directly relate to constraints on torque generation as these might have allowed for the development of controlled gliding as a precursor for flight in a variety of organisms.

## Appendix A. Gaussian impulsive control

Through all of the analysis described in this paper, the control action has been identified by a torque applied to the system centre of mass via an internal rotor. Of course, this hypothesis will apparently fail if one observes that animals cannot apply torque in the same way that an internal rotor does. In particular, animals such as gliding ants can only apply impulsive torque, for example by moving their legs. This is clearly in contrast to the ‘constant torque control’ used in §§ 3 and 4 and thus it is crucial to analyse the limit of the described analysis.

In particular, the relative weight between the exact ‘shape’ of the torque with respect to its average value has to be evaluated. To this end, a periodic Gaussian torque has been applied to the system. Each impulse is described by the function

$$\tau(t) = \hat{\tau} e^{-(t-t_d)^2/2\sigma^2}, \quad (\text{A } 1)$$

where  $\sigma$  sets the width, the peak torque is identified by  $\hat{\tau}$  and the forcing period is indicated by  $T_\tau$ . Moreover, a time shift  $t_d$  has been introduced to maximize the control efficiency, as discussed in the following.

By keeping the average torque

$$\tau_0 = \frac{1}{T_\tau} \int_0^{T_\tau} \tau \, dt \simeq \frac{1}{T_\tau} \sqrt{2\pi} \hat{\tau} \sigma \quad (\text{A } 2)$$

constant, we analyse the dependence of  $\langle w \rangle$  on  $\hat{\tau}$  and  $T_\tau$ . Note that  $\hat{\tau}$  and  $T_\tau$  are related by (A 2) where the last equality holds if the Gaussian impulses do not overlap, i.e. if

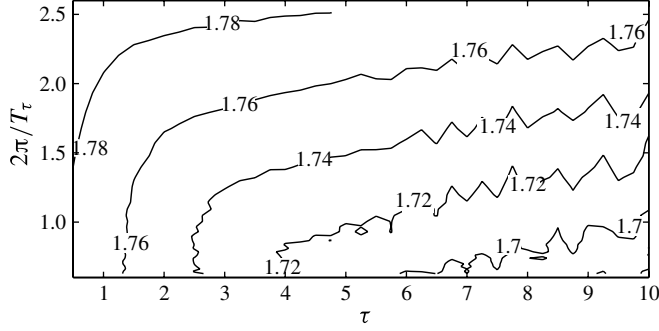
$$6\sigma < T_\tau \Rightarrow \frac{6\tau_0 T_\tau}{\sqrt{2\pi} \hat{\tau}} < T_\tau \Rightarrow T_\tau \left( 1 - \frac{6\tau_0}{\sqrt{2\pi} \hat{\tau}} \right) > 0, \quad (\text{A } 3)$$

thus we will limit our analysis only for these cases. On the other hand, if

$$T_\tau \left( 1 - \frac{6\tau_0}{\sqrt{2\pi} \hat{\tau}} \right) \ll 0 \quad (\text{A } 4)$$

the Gaussian impulses overlap, therefore the torque has a predominant DC component and the analysis of § 3 holds. The additional degree of freedom provided by the relative phasing  $t_d$  between the angular position of the ellipse and the impulse can be exploited to maximize the control efficiency by synchronizing the impulse with the rotation of the body.

The dependence of  $\langle w \rangle = w_0$  on  $\hat{\tau}$  and  $T_\tau$  with  $\tau_0 = 1$  is reported in figure 8. For plotting purposes we report the value of  $w_0$  given by the most efficient  $t_d$  for every point  $(\hat{\tau}, T_\tau)$ . Note that, although the period of excitation can be as large as twice the period of rotation of the ellipse and the maximum torque amplitude spans an order of magnitude, the resulting rotational velocity  $w_0$  changes by only about 5%. Thus, the

FIGURE 8. Dependence of  $w_0$  on  $\hat{\tau}$  and  $T_\tau$  ( $\tau_0 = 1$ ).

hypothesis that only the average torque influences the system dynamics is appropriate for this system.

### Appendix B. Drag force nonlinearities

The estimation of  $\theta_0$  from (3.25) requires us to calculate an expression for the first harmonic approximation  $F_1^c$  of the drag force nonlinearities, i.e. what is known in control theory as the describing function of those nonlinearities. For large  $I$ , i.e. when the aspect ratio is bigger than the density ratio  $\rho_f/\rho_s$ ,  $\kappa \simeq -1$  and thus  $u_1^c \simeq -v_1^s$ . Within this assumption the drag force nonlinearities can then be approximated as

$$\begin{aligned}
 \sqrt{u^2 + v^2} u &= \sqrt{u_1^c{}^2 \cos^2(w_0 t) + v_1^s{}^2 \sin^2(w_0 t)} u_1^c \cos(w_0 t) \\
 &= \sqrt{\kappa^2 v_1^s{}^2 \cos^2(w_0 t) + v_1^s{}^2 \sin^2(w_0 t)} (-\kappa v_1^s) \cos(w_0 t) \\
 &= -\sqrt{1 + (\epsilon^2 + 2\epsilon) \cos^2(w_0 t)} |v_1^s| \kappa v_1^s \cos(w_0 t) \\
 &\simeq -\kappa |v_1^s| v_1^s \cos(w_0 t) - \kappa |v_1^s| v_1^s \frac{\epsilon^2 + 2\epsilon}{2} \cos^2(w_0 t) \cos(w_0 t) \\
 &= -\kappa |v_1^s| v_1^s \left\{ \left( 1 + \frac{3\epsilon^2 + 2\epsilon}{4} \right) \cos(w_0 t) + \frac{1\epsilon^2 + 2\epsilon}{4} \cos(3w_0 t) \right\} \\
 &= -\kappa |v_1^s| v_1^s \left\{ \left( \frac{5}{8} + \frac{3}{8}\kappa^2 \right) \cos(w_0 t) + \frac{-1 + \kappa^2}{8} \cos(3w_0 t) \right\} \quad (\text{B } 1)
 \end{aligned}$$

$$\begin{aligned}
 \frac{u^2 - v^2}{u^2 + v^2} \sqrt{u^2 + v^2} u &= -\frac{u_1^c{}^2 \cos^2(w_0 t) - v_1^s{}^2 \sin^2(w_0 t)}{u_1^c{}^2 \cos^2(w_0 t) + v_1^s{}^2 \sin^2(w_0 t)} |v_1^s| \kappa v_1^s \\
 &\quad \times \left( 1 + \frac{\epsilon^2 + 2\epsilon}{2} \cos^2(w_0 t) \right) \cos(w_0 t) \\
 &= -\frac{\kappa^2 \cos^2(w_0 t) - \sin^2(w_0 t)}{\kappa^2 \cos^2(w_0 t) + \sin^2(w_0 t)} \kappa |v_1^s| v_1^s \\
 &\quad \times \left( 1 + \frac{\epsilon^2 + 2\epsilon}{2} \cos^2(w_0 t) \right) \cos(w_0 t) \\
 &= -\frac{(1 + \epsilon^2 + 2\epsilon) \cos^2(w_0 t) - (1 - \cos^2(w_0 t))}{(1 + \epsilon^2 + 2\epsilon) \cos^2(w_0 t) + (1 - \cos^2(w_0 t))}
 \end{aligned}$$

$$\begin{aligned}
& \times \kappa |v_1^s| v_1^s \left( 1 + \frac{\epsilon^2 + 2\epsilon}{2} \cos^2(w_0 t) \right) \cos(w_0 t) \\
& = - \frac{2\cos^2(w_0 t) - 1 (\epsilon^2 + 2\epsilon) \cos^2(w_0 t)}{1 + (\epsilon^2 + 2\epsilon) \cos^2(w_0 t)} \kappa |v_1^s| v_1^s \\
& \quad \times \left( 1 + \frac{\epsilon^2 + 2\epsilon}{2} \cos^2(w_0 t) \right) \cos(w_0 t) \\
& \simeq - \left\{ 1 + \cos(2w_0 t) - 1 + \frac{\epsilon^2 + 2\epsilon}{2} + \frac{\epsilon^2 + 2\epsilon}{2} \cos(2w_0 t) \right\} \\
& \quad \times \kappa |v_1^s| v_1^s \left( 1 + \frac{\epsilon^2 + 2\epsilon}{2} \cos^2(w_0 t) \right) \cos(w_0 t) \\
& = - \left\{ \frac{1 + \kappa^2}{2} + \left( 1 + \frac{1 + \kappa^2 - 2}{2} \right) \cos(2w_0 t) \right\} \kappa |v_1^s| v_1^s \\
& \quad \times \left\{ 1 + \frac{1 + \kappa^2 - 2}{2} + \frac{1 + \kappa^2 - 2}{2} \cos(2w_0 t) \right\} \cos(w_0 t) \\
& = - \left\{ -\frac{3}{16} + \frac{11}{16} \kappa^4 \right\} \kappa |v_1^s| v_1^s \cos(w_0 t) \\
& \quad - \left\{ \frac{3}{16} + \frac{5}{16} \kappa^4 \right\} \kappa |v_1^s| v_1^s \cos(3w_0 t) \tag{B 2}
\end{aligned}$$

where  $\epsilon = -1 - \kappa$  and the approximate relation  $\sqrt{1+x} \simeq 1 + (x/2)$  when  $x \ll 1$  has been exploited.

By using these approximate expressions in the harmonic balance equation one obtains the following equation for  $\sin \theta_0$

$$\begin{aligned}
& \left[ -A \left( \frac{5}{8} + \frac{3}{8} \kappa^2 \right) + B \left( -\frac{3}{16} + \frac{11}{16} \kappa^4 \right) \right] \frac{\kappa \pi^2}{4C_R^2 w_0^2} \text{sign} \left( \frac{\cos \theta_0}{w_0} \right) \\
& - \left[ -A \left( \frac{5}{8} + \frac{3}{8} \kappa^2 \right) + B \left( -\frac{3}{16} + \frac{11}{16} \kappa^4 \right) \right] \\
& \quad \times \frac{\kappa \pi^2}{4C_R^2 w_0^2} \text{sign} \left( \frac{\cos \theta_0}{w_0} \right) \sin^2 \theta_0 + \sin \theta_0 = 0. \tag{B 3}
\end{aligned}$$

Moreover, thanks to the symmetry of the system,  $\theta_0$  can be chosen such that  $\cos \theta_0$  is always positive and therefore we can write the unique solution of (B 3) as in (3.37).

## Appendix C. Optimality test

In order to test the quality of the optimal trajectories obtained by the numerical algorithm, we compare them with the optimality necessary conditions provided by the Pontryagin maximum principle. To this end, an analytical expression of such conditions is derived and a comparison between them and the obtained trajectories is reported.

First of all, note that the symmetry of the system implies that the constraint about final orientation can be imposed only mod( $2\pi$ ), however the ‘mod’ function introduces a discontinuity around  $2\pi$  that can cause numerical problems during the optimization process. In order to overcome this problem and noting that  $\theta$  appears only as an argument of trigonometric functions, we define an auxiliary system with

(extended) state  $\tilde{X} = [u, v, w, x, v, \chi, \sigma, \tau]$  where  $\chi(t) = \cos \theta(t)$  and  $\sigma(t) = \sin \theta(t)$ . The auxiliary system dynamics can then be written as, on dropping the tilde and with a little abuse of notation,

$$\dot{X} = G_0(X) + JG_1(X) \quad (C1)$$

$$G_0(X) = \begin{bmatrix} ((I+1)vw - \Gamma v - \sigma - F)(I + \beta^2)^{-1} \\ -(I + \beta^2)uw + \Gamma u - \chi - G)(I + 1)^{-1} \\ ((\beta^2 - 1)uv + \tau - M) \left( \frac{1}{4} \left( I(1 + \beta^2) + \frac{1}{2} (1 - \beta^2)^2 \right) \right)^{-1} \\ u\chi - v\sigma \\ u\sigma + v\chi \\ -\sigma w \\ \chi w \\ 0 \end{bmatrix} \quad (C2)$$

$$G_1 = \begin{bmatrix} 0 & 0 & 0 & 0 & 0 & 0 & 0 & 1 \end{bmatrix}^T. \quad (C3)$$

Note that the dimension of the state space for the auxiliary system is increased by one with respect to the original system, but now the boundary conditions can be imposed by means of smooth functions. The related optimal control problem can now be stated as

$$\min_J \mathcal{C} = \min_J \int_0^T [1 + \eta (\tau^2 + \alpha J^2)] dt \quad (C4)$$

$$\dot{X} = G_0(X) + G_1 J \quad (C5)$$

$$X(0) = X_0 \quad (C6)$$

$$X(T) \in \mathcal{F} \quad (C7)$$

$$\mathcal{F} = \{X(T) \in \mathbb{R}^8 : x(T) = x_f, y(T) = y_f, \chi(T) = \chi_f, \sigma(T) = \sigma_f, |\dot{x}(T)| \leq \dot{x}_{max}, |\dot{y}(T)| \leq \dot{y}_{max}, |w(T)| \leq w_{max}\} \quad (C8)$$

$$|\tau| \leq \tau_{max} \quad (C9)$$

$$|J| \leq J_{max}. \quad (C10)$$

To check the quality of the solutions provided by the numerical algorithm we compare them with the optimality necessary conditions given by the Pontryagin maximum principle. It is known that for  $N \rightarrow +\infty$  the approximate solutions satisfy the Pontryagin conditions, but in practice one cannot increase  $N$  too much due to computational complexity issues and therefore it is useful to check how far the candidate trajectories are from satisfying the analytical optimality conditions.

Let us now use the Pontryagin maximum principle to derive such necessary conditions for optimality. The first step consists of defining the so-called Pontryagin Hamiltonian

$$H(X, \Lambda; J) = \Lambda_0 [1 + \eta (\tau^2 + \alpha J^2)] + \Lambda \cdot [G_0(X) + G_1 J] - \mu \cdot c(x, u, t) \quad (C11)$$

or, more explicitly,

$$\begin{aligned} H = & \Lambda_0 [1 + \eta (\tau^2 + \alpha J^2)] \\ & + \Lambda_1 \{(I+1)vw - \Gamma v - \sigma - F\} (I + \beta^2)^{-1} \\ & + \Lambda_2 \{(-I - \beta^2)uw + \Gamma u - \chi - G\} (I + 1)^{-1} \end{aligned}$$

$$\begin{aligned}
& + \Lambda_3 \frac{(\beta^2 - 1)uv + \tau - M}{1/4I(1 + \beta^2) + 1/8(1 - \beta^2)^2} + \Lambda_4(u\chi - v\sigma) \\
& + \Lambda_5(u\sigma + v\chi) - \Lambda_6\sigma w + \Lambda_7\chi w + \Lambda_8 J - \mu(\tau^2 - \tau_{max}^2) \quad (C 12)
\end{aligned}$$

where  $\Lambda_0 \in \mathbb{R}^+$  and  $\Lambda : [0, T] \rightarrow \mathbb{R}^8$  are called adjoint variables or costates,  $c(x, u, t) = \tau^2 - \tau_{max}^2 \leq 0$  represents the path constraints and  $\mu : [0, T] \rightarrow \mathbb{R}$  is a Lagrange multiplier associated with these constraints. The Pontryagin maximum principle states that the optimal trajectory  $(X^*, \Lambda^*)$  is associated with the vector field  $\bar{H}^*$  such that the following conditions hold:

(a) minimality condition:

$$H^* = H(X^*, \Lambda^*; J^*) = \min_{|J| \leq J_{max}} H(X^*, \Lambda^*; J) \quad (C 13)$$

(b) free final time condition:

$$H^* \equiv 0 \quad \forall t \in [0, T] \quad (C 14)$$

(c) non-triviality of solution:

$$|\Lambda(t)| \neq 0 \quad \forall t \in [0, T] \quad (C 15)$$

(d) path constraint condition:

$$\mu = 0 \quad \text{if } c(x, u, t) < 0 \quad (C 16)$$

$$\mu \leq 0 \quad \text{if } c(x, u, t) = 0 \quad (C 17)$$

(e) transversality condition:

$$\forall \delta \in T_{X(T)}\mathcal{F} \quad \Lambda(T) \cdot \delta = 0 \quad (C 18)$$

where  $T_{X(T)}\mathcal{F}$  represents the tangent space of  $\mathcal{F}$  at the point  $X(T)$ .

Owing to the particular structure of  $G_1$  and of the performance index  $\mathcal{C}$ , the minimality condition (C 13) reduces to

$$J^* = \arg \min_{|J| \leq J_{max}} \{ \Lambda_0 \eta \alpha J^2 + \Lambda_8 J \} \quad (C 19)$$

and therefore the optimal control  $J^*$  can be written as

$$J^* = \begin{cases} -\frac{\Lambda_8}{2\Lambda_0\eta\alpha} - J_{max} \leq -\frac{\Lambda_8}{2\Lambda_0\eta\alpha} \leq J_{max}, \Lambda_0\eta\alpha \neq 0 \\ -J_{max} - \frac{\Lambda_8}{2\Lambda_0\eta\alpha} < -J_{max}, \text{ or } \Lambda_0\eta\alpha = 0, \Lambda_8 > 0 \\ J_{max} - \frac{\Lambda_8}{2\Lambda_0\eta\alpha} > J_{max}, \text{ or } \Lambda_0\eta\alpha = 0, \Lambda_8 < 0. \end{cases} \quad (C 20)$$

Note that if  $\Lambda_0 \neq 0$ , the adjoint variables can always be normalized such that  $\Lambda_0 = 1$  due to the homogeneous nature of the Hamiltonian  $H$ . Trajectories with  $\Lambda_0 = 0$  are called abnormal trajectories and represent quite pathological situations because their optimality does not depend on the performance index. In the following we focus only on normal trajectories, i.e. we always consider  $\Lambda_0 = 1$ .

As  $\eta\alpha \rightarrow 0$  and  $\Lambda_8 \neq 0$ , (C 20) implies bang-bang trajectories, as usual in time-minimum problems with affine-in-control dynamics. However, in our model bang-bang trajectories could also arise in the energy-optimal perching problem with  $\alpha = 0$ . Trajectories with  $\Lambda_8 = 0, \eta\alpha = 0$  on a finite time interval  $[t_1, t_2]$  are called singular

trajectories and an alternative expression for the input is needed. Necessary conditions for the existence of singular trajectories are, by definition,

$$\Lambda_8(t) \equiv 0, \quad \dot{\Lambda}_8(t) \equiv \ddot{\Lambda}_8 \equiv \dots \equiv 0, \quad t \in [t_1, t_2]. \quad (\text{C } 21)$$

By exploiting the relation

$$\frac{d\Lambda}{dt} = -\frac{\partial H}{\partial X} \quad (\text{C } 22)$$

we can rewrite conditions (C 21) in the energy-optimal case as

$$\dot{\Lambda}_8 = -2\Lambda_0\eta\tau - \frac{\Lambda_3}{\frac{1}{4}I(1+\beta^2) + \frac{1}{8}(1-\beta^2)^2} = 0, \quad (\text{C } 23)$$

$$\ddot{\Lambda}_8 = 2\Lambda_0\eta J - \frac{\dot{\Lambda}_3}{\frac{1}{4}I(1+\beta^2) + \frac{1}{8}(1-\beta^2)^2} = 0, \quad (\text{C } 24)$$

$$\Rightarrow J = -\frac{\dot{\Lambda}_3}{2\Lambda_0\eta \left[ \frac{1}{4}I(1+\beta^2) + \frac{1}{8}(1-\beta^2)^2 \right]}. \quad (\text{C } 25)$$

The analysis of singular trajectories in the time-optimal case is much more involved due to the lack of the first term ( $\eta = 0$ ) and requires considering all of the derivatives of  $\Lambda_8$  up to the fourth. However, note that in the time-optimal trajectories obtained by numerical algorithm  $J$  is different from  $\pm J_{\max}$  only when the path constraints are active, i.e.  $\tau = \pm\tau_{\max}$ , and in this case the control must be zero thanks to the relation  $\dot{\tau} = J$ .

The transversality conditions (C 18) imply some constraints on the adjoint variables final values. In fact, depending on which set of constraints is active, different orthogonality conditions between the vector  $\Lambda$  and the tangent space  $T_{X(T)}\mathcal{F}$  arise. Then let us define

$$g_1(X(T)) = \dot{x}^2(T) - \dot{x}_{\max}^2 = (u(T)\chi_f - v(T)\sigma_f)^2 - \dot{x}_{\max}^2, \quad (\text{C } 26)$$

$$g_2(X(T)) = \dot{y}^2(T) - \dot{y}_{\max}^2 = (u(T)\sigma_f + v(T)\chi_f)^2 - \dot{y}_{\max}^2, \quad (\text{C } 27)$$

$$g_3(X(T)) = \dot{w}^2(T) - w_{\max}^2, \quad (\text{C } 28)$$

so that the final set  $\mathcal{F}$  can be expressed as

$$\mathcal{F} = \{X(T) \in \mathbb{R}^8 : g_1 \leq 0, g_2 \leq 0, g_3 \leq 0, x(T) = x_f, y(T) = y_f, \chi(T) = \chi_f, \sigma(T) = \sigma_f\}. \quad (\text{C } 29)$$

Note that  $g_3$  involves only one state variable, thus only two cases must be considered:

- (a)  $g_3 < 0$ , then  $\Lambda_3(T) = 0$  as if  $w(T)$  was free;
- (b)  $g_3 = 0$ , then  $w(T)$  is fixed at  $\pm w_{\max}$  and  $\Lambda_3$  is free.

On the other hand,  $g_1$  and  $g_2$  involve both  $u$  and  $v$ , therefore they will influence the values of  $\Lambda_1(T)$  and  $\Lambda_2(T)$  and four subcases can occur:

- (a)  $g_1 < 0, g_2 < 0$ , then  $\Lambda_1(T) = \Lambda_2(T) = 0$  as if  $u, v$  were free;
- (b)  $g_1 = 0, g_2 < 0$ , then  $|u(T)\chi_f - v(T)\sigma_f| = \dot{x}_{\max}$ . When  $g_1 = 0$ , then  $\nabla g_1$  is a vector orthogonal to the boundary of  $\mathcal{F}$  and reads

$$\nabla g_1 = [\pm \dot{x}_{\max}\chi_f, \mp \dot{x}_{\max}\sigma_f, 0, 0, 0, 0, 0, 0], \quad (\text{C } 30)$$



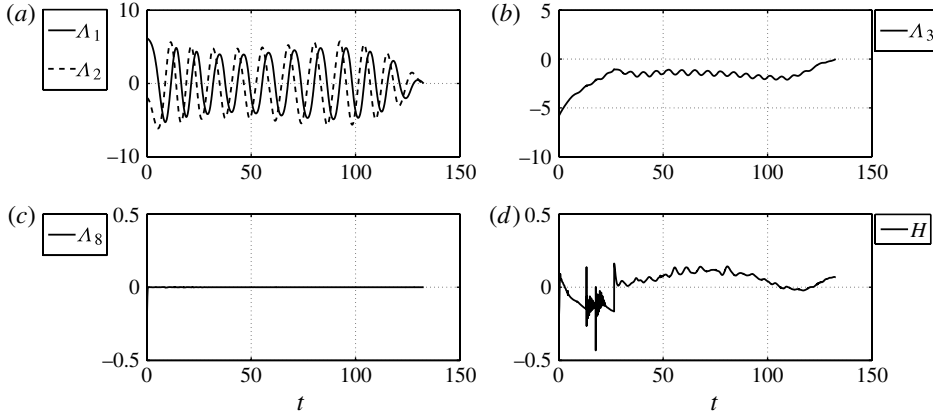


FIGURE 9. Costate dynamics (a–c) and Pontryagin Hamiltonian (d) for energy-optimal trajectory without bounds on final velocities reported in figure 6(a,b) ( $\dot{x}_{\max} = \dot{y}_{\max} = w_{\max} \rightarrow +\infty$ ,  $N = 600$ ). We note that  $\Lambda_1(T) = \Lambda_2(T) = \Lambda_3(T) = 0$  in agreement with the analysis in the absence of final velocities constraints and that the trajectory is almost purely singular because  $\Lambda_8(t) = 0$  for  $t > 0.4$ . The number  $N$  of points has been chosen so that the Hamiltonian magnitude is small throughout the trajectory.

thus  $\Lambda_1(T)$  and  $\Lambda_2(T)$  have to satisfy the relation

$$-\sigma_f \Lambda_1(T) = \chi_f \Lambda_2(T). \quad (\text{C } 31)$$

(c)  $g_1 < 0$ ,  $g_2 = 0$  then, by analogous reasoning, one obtains

$$\chi_f \Lambda_1(T) = \sigma_f \Lambda_2(T). \quad (\text{C } 32)$$

(d)  $g_1 = g_2 = 0$ , then  $u$  and  $v$  are fixed and therefore  $\Lambda_1$  and  $\Lambda_2$  are free.

The other constraints on the final state of the system are more simple to handle and imply

$$\Lambda_8(T) = 0, \quad (\text{C } 33)$$

$$\Lambda_4(T), \Lambda_5(T), \Lambda_6(T), \Lambda_7(T) \text{ free.} \quad (\text{C } 34)$$

The relevant adjoint variables and Pontryagin Hamiltonian for the trajectories without final velocities constraints reported in the paper are plotted, respectively, in figures 9 and 10.

All of the transversality conditions are correctly satisfied, in fact  $\Lambda_1(T) = \Lambda_2(T) = \Lambda_3(T) = \Lambda_8(T) = 0$  in both cases. Moreover,  $\Lambda_4$  and  $\Lambda_5$  are both constant in both cases as requested (data not shown). From these plots it also becomes evident that the energy-optimal trajectory is a purely singular trajectory because  $\Lambda_8 = 0$  during the whole trajectory. The approximate nature of the solutions becomes evident by inspecting the behaviour of the Pontryagin Hamiltonian. In fact, according to the Pontryagin maximum principle, the Hamiltonian should be constant and equal to zero during the whole trajectory, but the results from the GPOPS algorithm do not exactly satisfy this condition. Increasing the number of grid points  $N$  can mitigate this problem but the computational time quickly increases. The number of points  $N$  has thus been chosen such that the Hamiltonian magnitude is close to zero along the whole trajectory and, moreover, the trajectory itself does not differ substantially from that obtained on the coarser grid used in the previous step. Note that the magnitude of deviations from zero of the Hamiltonian is larger for time-optimal trajectories, but

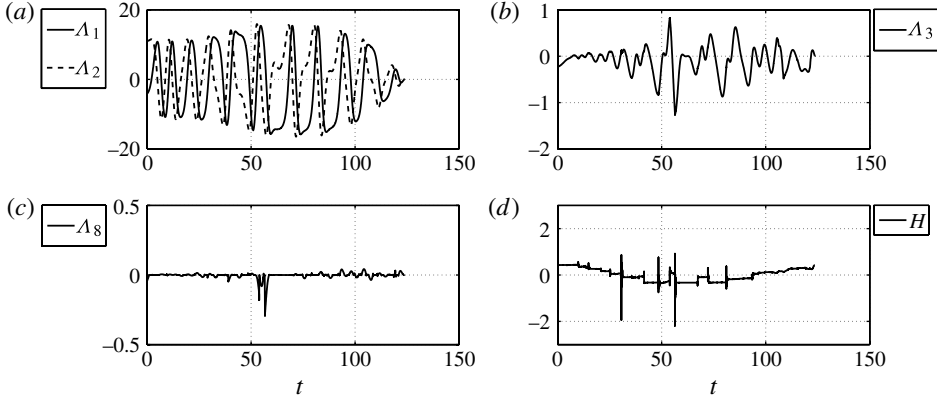


FIGURE 10. Costate dynamics (a–c) and Pontryagin Hamiltonian (d) for time-optimal trajectory without bounds on final velocities reported in figure 7(a,b) ( $\dot{x}_{\max} = \dot{y}_{\max} = w_{\max} \rightarrow +\infty$ ,  $N = 3500$ ). We note that  $\Lambda_1(T) = \Lambda_2(T) = \Lambda_3(T) = 0$  in agreement with the analysis in the absence of final velocities constraints. The number  $N$  of points has been chosen so that the Hamiltonian magnitude is small throughout the trajectory.

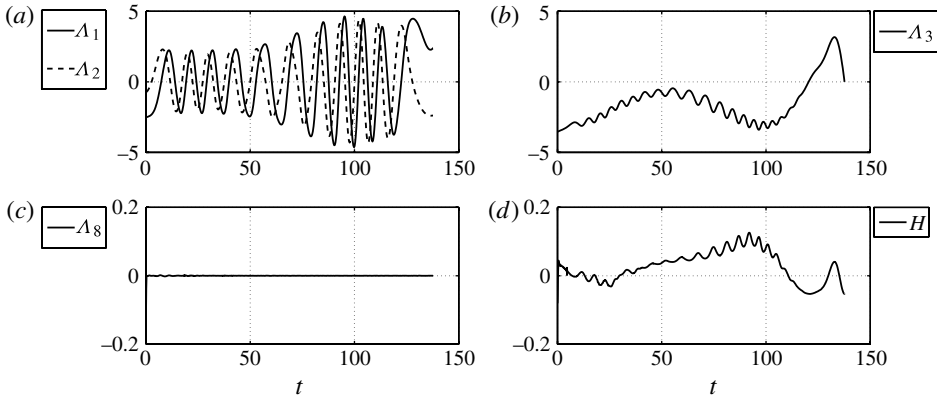


FIGURE 11. Costate dynamics (a–c) and Pontryagin Hamiltonian (d) for energy-optimal trajectory with bounds on final velocities  $\dot{x}_{\max} = \dot{y}_{\max} = w_{\max} = 0.5$  reported in figure 6(c–d) ( $N = 600$ ). We note that  $\Lambda_1(T) = -\Lambda_2(T)$  and  $\Lambda_3(T) = 0$  in agreement with the analysis in presence of final velocities constraints and that the trajectory is almost purely singular because  $\Lambda_8(t) = 0$  for  $t > 0.3$ . The number  $N$  of points has been chosen so that the Hamiltonian magnitude is small throughout the trajectory.

this is due to the slower rate of convergence of the algorithm for bang–bang control and the number of points could not be further increased due to computational time constraints. However, also in the time-optimal case the actual trajectory of the system nearly overlaps to that obtained on a coarser grid and thus we are very close to complete convergence.

The adjoint variables and the Pontryagin Hamiltonian associated with energy- and time-optimal trajectories in presence of bounds on final velocities are reported in figures 11 and 12.

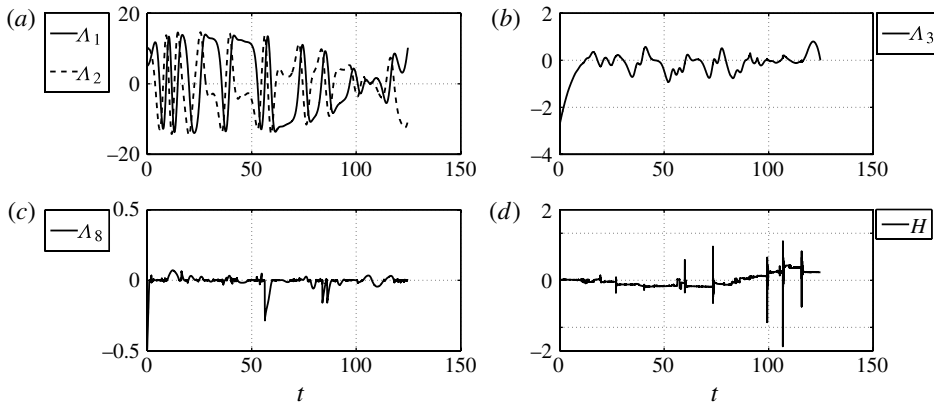


FIGURE 12. Costate dynamics (a–c) and Pontryagin Hamiltonian (d) for time-optimal trajectory without bounds on final velocities  $\dot{x}_{\max} = \dot{y}_{\max} = w_{\max} = 0.5$  reported in figure 7(c–d) ( $N = 3500$ ). We note that  $\Lambda_1(T) = -\Lambda_2(T)$  and  $\Lambda_3(T) = 0$  in agreement with the analysis in the absence of final velocities constraints. The number  $N$  of points has been chosen so that the Hamiltonian magnitude is small throughout the trajectory.

The discussion reported for the unbounded final velocity trajectories still holds with the exception of the transversality conditions that have to be modified to take into account the presence of a bound on the final velocity. Note that in this case  $\Lambda_1(T) = -\Lambda_2(T)$  as predicted by (C31) with  $\sigma_f = \chi_f$  ( $\theta = \pi/4$ ).

#### REFERENCES

- ANDERSEN, A., PESAVENTO, U. & WANG, Z. J. 2005a Analysis of transitions between fluttering, tumbling and steady descent of falling cards. *J. Fluid Mech.* **541**, 91–104.
- ANDERSEN, A., PESAVENTO, U. & WANG, Z. J. 2005b Unsteady aerodynamics of fluttering and tumbling plates. *J. Fluid Mech.* **541**, 65–90.
- BELMONTE, A., EISENBERG, H. & MOSES, E. 1998 From flutter to tumble: inertial drag and froude similarity in falling paper. *Phys. Rev. Lett.* **81** (2), 345–348.
- BENSON, D. A. 2004 A Gauss pseudospectral transcription for optimal control. PhD thesis, Department of Aeronautics and Astronautics, MIT.
- BENSON, D. A., HUNTINGTON, G. T., THORVALDSEN, T. P. & RAO, A. V. 2006 Direct Trajectory Optimization and Costate Estimation via an Orthogonal Collocation Method. *J. Guid. Control Dyn.* **29** (6), 1435–1440.
- BRADLEY, T. J., BRISCOE, A. D., BRADY, S. G., CONTRERAS, H. L., DANFORTH, B. N., DUDLEY, R., GRIMALDI, D., HARRISON, J. F., KAISER, J. A., MERLIN, C., REPERT, S. M., VANDENBROOKS, J. M. & YANOVIK, S. P. 2009 Episodes in insect evolution. *Integr. Compar. Biol.* **49** (5), 590–606.
- CORY, R. & TEDRAKE, R. 2008 Experiments in fixed-wing UAV perching. In *AIAA Guidance, Navigation, and Control Conference*.
- DUDLEY, R. 2000 *The Biomechanics of Insect Flight: Form, Function, Evolution*. Princeton University Press.
- DUDLEY, R., BYRNES, G., YANOVIK, S. P., BORRELL, B., BROWN, R. M. & MCGUIRE, J. A. 2007 Gliding and the functional origins of flight: biomechanical novelty or necessity? *Annu. Rev. Ecol. Evol. Systemat.* **38** (1), 179–201.
- GARG, D., PATTERSON, M. A., HAGER, W. W., RAO, A. V., BENSON, D. A. & HUNTINGTON, G. T. 2010 A unified framework for the numerical solution of optimal control problems using pseudospectral methods. *Automatica* **46** (11), 1843–1851.
- GILL, P. E., MURRAY, W. & SAUNDERS, M. A. 2005 SNOPT: an SQP algorithm for large-scale constrained optimization. *SIAM Rev.* **47** (1), 99–131.

- GRIMALDI, D. A. & ENGEL, M. S. 2005 *Evolution of the Insects*. Cambridge University Press.
- HASENFUSS, I. 2008 The evolutionary pathway to insect flight – a tentative reconstruction. *Arthropod Systemat. Phylogeny* **66** (1), 19–35.
- HUNTINGTON, G. T. 2007 Advancement and analysis of a gauss pseudospectral transcription for optimal control. PhD thesis, Dept. of Aeronautics and Astronautics, MIT.
- HUNTINGTON, G. T., BENSON, D. A. & RAO, A. V. 2007a Design of optimal tetrahedral spacecraft formations. *J. Astronautical Sci.* **55** (2), 141–169.
- HUNTINGTON, G. T., BENSON, D. A., HOW, J. P., KANIZAY, N., DARBY, C. L. & RAO, A. V. 2007b Computation of boundary controls using a gauss pseudospectral method. In *2007 Astrodynamic Specialist Conference, Mackinac Island, Michigan*.
- HUNTINGTON, G. T. & RAO, A. V. 2008 Optimal reconfiguration of spacecraft formations using a gauss pseudospectral method. *J. Guid. Control Dyn.* **31** (3), 689–698.
- JACKSON, S. M. 2000 Glide angle in the genus *petaurus* and a review of gliding in mammals. *Mammal Rev.* **30** (1), 9–30.
- KIRK, D. E. 2004 *Optimal Control Theory: An Introduction*. Dover.
- LAMB, H. 1945 *Hydrodynamics*. Dover.
- MAHADEVAN, L. 1996 Tumbling of a falling card. *C. R. Acad. Sci. Sér. II* **323**, 729–736.
- MAHADEVAN, L., RYU, W. S. & ARAVINTHAN, D. T. S. 1999 Tumbling cards. *Phys. Fluids* **11**, 1–3.
- MITTAL, R., SESHADRI, V. & UDAYKUMAR, H. S. 2004 Flutter, tumble and vortex induced autorotation. *Theor. Comput. Fluid Dyn.* **17** (3), 165–170.
- PESAVENTO, U. & WANG, Z. J. 2004 Falling paper: Navier–Stokes solutions, model of fluid forces, and centre of mass elevation. *Phys. Rev. Lett.* **93** (14), 144501.
- PONTRYAGIN, L. S., BOLTYANSKII, V. G., GAMKRELIDZE, R. V. & MISCHENKO, E. F. 1962 *The Mathematical Theory of Optimal Processes*. Wiley-Interscience.
- RAO, A. V., BENSON, D. A., DARBY, C. L., PATTERSON, M. A., FRANCOLIN, C. & HUNTINGTON, G. T. 2010 Algorithm 902: GPOPS, a MATLAB software for solving multiple-phase optimal control problems using the Gauss pseudospectral method. *ACM Trans. Math. Softw.* **37** (2), 22:1–39.
- RAYNER, J. M. V. 1985 Bounding and undulating flight in birds. *J. Theor. Biol.* **117**, 47–77.
- ROBERTS, JOHN W., CORY, RICK & TEDRAKE, RUSS 2009 On the controllability of fixed-wing perching. In *Proceedings of the American Controls Conference (ACC)*.
- TOBALSKE, B. W. 2010 Hovering and intermittent flight in birds. *Bioinspiration Biomimetics* **5** (4), 045004.
- WANG, Z. J., BIRCH, J. M. & DICKINSON, M. H. 2004 Unsteady forces and flows in low Reynolds number hovering flight: two-dimensional computations vs robotic wing experiments. *J. Expl. Biol.* **207** (3), 449–460.
- WOOLSEY, C. A. & LEONARD, N. E. 2002 Moving mass control for underwater vehicles. *Proceedings of the 2002 American Control Conference*, vol. 4, pp. 2824–2829.
- YANOVIK, S. P., DUDLEY, R. & KASPARI, M. 2005 Directed areal descent in canopy ants. *Nature* **433**, 624–626.
- YANOVIK, S., FISHER, B. & ALONSO, A. 2008 Directed Aerial Descent Behavior in African Canopy Ants (Hymenoptera: Formicidae). *J. Insect Behavior* **21** (3), 164–171.
- YANOVIK, S. P., KASPARI, M. & DUDLEY, R. 2009 Gliding hexapods and the origins of insect aerial behaviour. *Biol. Lett.* **5** (4), 510–512.
- YANOVIK, S. P., MUNK, Y., KASPARI, M. & DUDLEY, R. 2010 Aerial manoeuvrability in wingless gliding ants (*Cephalotes atratus*). *Proc. R. Soc. B Biol. Sci.* **277** (1691), 2199–2204.